

5G PRS-Based Sensing: A Sensing Reference Signal Approach for Joint Sensing and Communication System

Zhiqing Wei, Yuan Wang, Liang Ma, Shaoshi Yang, Zhiyong Feng, Chengkang Pan, Qixun Zhang, Yajuan Wang, Huici Wu, Ping Zhang

Abstract

The emerging joint sensing and communication (JSC) technology is expected to support new applications and services, such as autonomous driving and extended reality (XR), in the future wireless communication systems. Pilot (or reference) signals in wireless communications usually have good passive detection performance, strong anti-noise capability and good auto-correlation characteristics, hence they bear the potential for applying in radar sensing. In this paper, we investigate how to apply the positioning reference signal (PRS) of the 5th generation (5G) mobile communications in radar sensing. This approach has the unique benefit of compatibility with the most advanced mobile communication system available so far. Thus, the PRS can be regarded as a sensing reference signal to simultaneously realize the functions of radar sensing, communication and positioning in a convenient manner. Firstly, we propose a PRS based radar sensing scheme and analyze its range and velocity estimation performance, based on which we propose a method that improves the accuracy of velocity estimation by using multiple frames. Furthermore, the Crámer-Rao lower bound (CRLB) of the range and velocity estimation for PRS based radar sensing and the CRLB of the range estimation for PRS based positioning are derived. Our analysis and simulation results demonstrate the feasibility and superiority of PRS over other pilot signals in radar sensing. Finally, some suggestions for the future 5G-Advanced and 6th generation (6G) frame structure design containing the sensing reference signal are derived based on our study.

Index terms— Joint Sensing and Communication, Integrated Sensing and Communication, 5G New Radio, 6G, Positioning Reference Signal, Sensing Reference Signal, Crámer-Rao lower bound

I. INTRODUCTION

The 5th generation advanced (5G-A) and 6th generation (6G) mobile communication systems are expected to support novel services such as autonomous driving, extended reality (XR), and so forth [1], which will require powerful communication and sensing capabilities simultaneously. Wireless sensing, including positioning, velocity detection and imaging, has long been an independent technology developed in parallel with mobile communications. In 5G-A and 6G mobile communication systems, millimeter wave (mmWave), terahertz (THz) and massive multi-input multi-output (MIMO) technologies could be indispensable. As a result, the frequency bands and antennas of wireless communication systems are becoming similar to those of radar, which makes the joint sensing and communication (JSC) technology feasible and promising [2]. In JSC, sensing and communication functions will be mutually beneficial in the same system, which can improve the spectral and energy efficiency while reducing the hardware cost. The application of JSC technology in future mobile networks has already become a consensus [3]. For example, the ITU IMT-2030 [4] has identified JSC as one of the candidate enabling technologies of 6G.

Waveform design is fundamental to the JSC technology. It imposes a strong impact on the performance of sensing and communication. The existing schemes can be divided into sensing centric waveforms and communication centric waveforms [5]. The sensing centric designs are based on the waveforms of radar,

Zhiqing Wei, Yuan Wang, Shaoshi Yang, Zhiyong Feng, Qixun Zhang, Huici Wu and Ping Zhang are with Beijing University of Posts and Telecommunications, Beijing, China 100876 (email: {weizhiqing, wangyuan, shaoshi.yang, fengzy, zhangqixun, dailywu, pzhang}@bupt.edu.cn) and Liang Ma, Chengkang Pan, Yajuan Wang are with Future Research Lab, China Mobile Research Institute, Beijing, China (email: {maliangyiy, panchengkang, wangyajuan}@chinamobile.com). *Correspondence author: Zhiqing Wei, Zhiyong Feng.*

such as the linear frequency modulated (LFM) signal [6] and the phase coded signal [7, 8]. However, the transmission rate of them is low. By contrast, the communication centric designs are based on the waveforms of wireless communications. So far, the orthogonal frequency division multiplexing (OFDM) has been widely applied in the design of communication centric JSC waveforms. For example, Sturm *et al.* [9, 10] first proposed a low-complexity signal processing algorithm to independently recover the range and Doppler information in an OFDM based radar system. Furthermore, according to the Shannon information theory [11], typically radar sensing needs structured waveforms with strong auto-correlation characteristics, while wireless communication requires random waveforms for maximizing the data rate. The pilot signals in wireless communication systems usually have good passive detection performance, strong anti-noise capability and good auto-correlation characteristics. Therefore, pilot signals with high auto-correlation have a great potential to be used in radar sensing, hence the JSC waveform design based on pilot signals has attracted much attention. There are various pilots designed for different purposes in the 5G standard, such as *synchronization signal (SS)*, *demodulation reference signal (DMRS)*, *channel state information-reference signal (CSI-RS)*, *positioning reference signal (PRS)*, and so on. Pilot based JSC waveforms have the following advantages: 1) In a JSC system, pilots can be used for radar sensing with low hardware cost and short implementation cycle; 2) The communication function and the pilot-based sensing function share resources in time domain or frequency domain, which can minimize the interference between radar and communication signals [12]; 3) The radar signal processing only needs to concentrate on the pilots, which reduces the computational complexity [13].

Pilot based JSC waveform design was mainly studied from the perspectives of pilot sequence selection [14, 15], pilot insertion mode [13, 16, 17], and time-frequency resource allocation [12, 13, 18]. In terms of pilot sequence selection, Kumari *et al.* [14] applied the preamble signal of the 802.11ad in radar sensing due to its good auto-correlation property. The Zadoff-Chu sequence with good auto-correlation was applied as the comb pilots of channel estimation to strike a balance between the communication error rate and the radar sensing performance in high mobility scenarios [15]. In terms of pilot insertion mode, Ozkaptan *et al.* [13] inserted the Barker code in a comb pilot, which was used in radar sensing and channel estimation to achieve high range and velocity resolution. The hardware-level verification in the 76-81 GHz frequency band for the design of [13] was provided in [16]. A JSC waveform using superimposed pilot and orthogonal space-time block code (OSTBC) precoding was proposed in [17], which is able to detect the target with large Doppler frequency shift. In terms of time-frequency resource allocation, [13] optimized subcarrier allocation to maximize the performance of radar sensing and communication under the constraints of radar estimation accuracy and effective channel capacity. The pilot based OFDM waveform is capable of realizing short-range, medium-range and long-range radars based on the flexible allocation of pilot subcarriers in [18]. A full-duplex communication and radar sensing system was designed in [12] using a frequency-division duplex scheme, where the data rate of communication was maximized by optimizing the power allocation of pilot signal.

However, the location of pilot subcarriers in [13] are rearranged in a stepped manner, and the superimposed pilot used in [17] introduces interference to the data by directly adding the pilot sequence to the data sequence, which does not meet the communication standard. In addition, the pilot in [14] is based on IEEE 802.11ad WLAN standard, while the OFDM system used in [13, 16, 18] is at 79 GHz carrier frequency and MHz large subcarrier frequency spacing to achieve high radar resolution, which makes them incompatible with 5G New Radio (NR) standard. In fact, there is a scarcity of work that directly investigate the use of the modern mobile communication signals of 5G and 5G-A in radar sensing [19]. The ITU-R WP5D Document [20] indicates that IMT-2030 and beyond will consider integrated communication, positioning and sensing, and potentially even jointly design flexible signals for concurrent communication, positioning and sensing with slight or no modification to hardware and waveform. Meanwhile, the sensing based positioning techniques can be further combined with the traditional reference signal based positioning techniques to improve the accuracy.

In this paper, considering that PRS is a signal specially designed for 5G in-band wireless positioning, we accomplish radar sensing using 5G PRS. Thus, PRS can be regarded as a *sensing reference signal* to

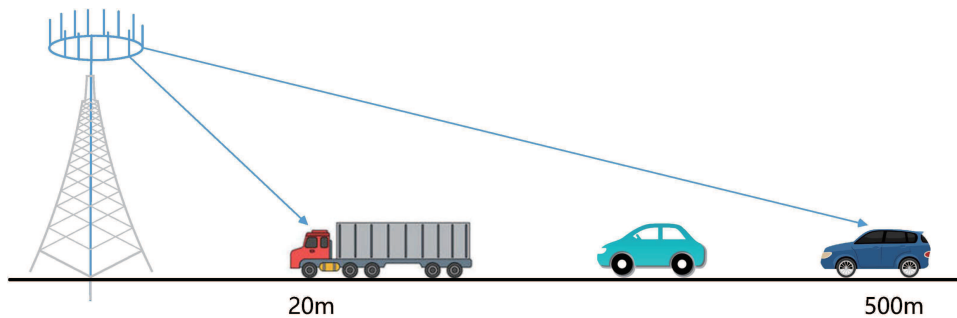


Fig. 1: JSC based roadside base station detecting vehicles

simultaneously realize the functions of radar sensing and positioning. PRS enjoys the advantages of long sequence, good auto-correlation, rich time-frequency resources and flexible configuration, which is more suitable for radar sensing compared with other pilot signals. The application of PRS in radar sensing does not require additional modification of communication signals, thus it is well compatible with 5G mobile communication systems, which is beneficial for promoting the integration of JSC technology in the coming 5G-A mobile communication system¹. As shown in Fig. 1, PRS is sent in the downlink to detect the target. The difficulty of engineering application may be the radar processing at the base station (BS). Due to the compatibility between the PRS based sensing and 5G communication system, there will be few modifications to the hardware. In 2021, Huawei completed the world's first verification of 5G-A JSC technology [21]. The test results show that the detection range of JSC base station exceeds 500 meters, which will provide an important reference for the integration of sensing capability at the base station. The main contributions of this paper are as follows.

1) We consider the downlink reference signals commonly used in 5G NR, namely SS, DMRS and CSI-RS, as comparisons to demonstrate the feasibility of PRS for radar sensing. Then the PRS based OFDM signal is applied as a JSC waveform, which can be regarded as the sensing reference signal. Our radar signal processing is focused on the pilot subcarriers to realize the range and velocity estimation, thus there is no need to make any changes to the 5G signal.

2) The Crámer-Rao lower bound (CRLB) of the range and velocity estimation concerning the PRS based sensing is derived, and the method of increasing the number of Fourier transform points [22] is applied to improve the accuracy of range and velocity estimation. In addition, an approach of velocity measurement using multiple frames is proposed to improve the accuracy of velocity estimation and reduce the time slot overhead within a frame.

3) The CRLB of PRS based positioning is derived. Positioning is the main sensing service provided by 5G mobile communication system. The multi-functional integration of sensing, communication, and positioning is realized with the aid of PRS.

4) Based on the above analysis, we give suggestions to the frame structure design in 5G-A and 6G. The sensing reference signal is configured in the frame to perform sensing tasks. The flexible deployment of sensing and communication overhead to satisfy the requirements of different scenarios, and the tradeoff between range and velocity estimation in radar sensing, are also discussed.

The rest of this paper is organized as follows. Section II introduces the PRS of 5G and evaluates its feasibility in radar sensing. Section III describes the system model of PRS based sensing. Section IV presents our proposed radar signal processing method based on PRS. The CRLBs of radar sensing and positioning relying on PRS are derived in Section V. Simulation results and discussions are presented in Section VI. The conclusions are drawn in Section VII. For convenience, the key parameters involved in this paper are listed in Table I.

¹5G-Advanced will start from 3GPP Release 18 (R18), which is expected to be frozen by the end of 2023. Hence, the sensing reference signal based JSC signal design will promote the rapid implementation of JSC technology.

TABLE I: Key Parameters

Symbol	Description
μ	Subcarrier spacing configuration
Δf	Frequency spacing of subcarriers
$N_{\text{ymb}}^{\text{slot}}$	Number of symbols per time slot
$N_{\text{slot}}^{\text{frame},\mu}$	Number of slots per frame for μ
T_{CP}	Length of the cyclic prefix
T	Duration of the OFDM symbol without cyclic prefix
T_s	Total duration of OFDM symbol
M	Number of OFDM symbols
N	Number of subcarriers
J	Set of subcarriers carrying PRS
N_J	Number of subcarriers carrying PRS
$K_{\text{comb}}^{\text{PRS}}$	Comb size of PRS
f_c	Carrier frequency
c	Speed of light
ξ	Attenuation factor
τ	Round-trip delay of target
R_r	Range of target
$f_{d,r}$	Doppler shift of target
v	Velocity of target
ΔR	Range resolution
R_{max}	Maximum unambiguous range
m_a	Fractional factor
Δv	Velocity resolution
v_{max}	Maximum unambiguous velocity
SNR	Signal-to-noise ratio

II. 5G POSITIONING REFERENCE SIGNAL

In this section, we introduce the PRS of 5G NR, and analyze its sequence correlation and time-frequency resource mapping scheme to evaluate its feasibility in radar sensing.

A. PRS Sequence Generation

The PRS sequence generating equation defined in TS 38.211 [23] is as follows.

$$r(m) = \frac{1}{\sqrt{2}}(1 - 2c(2m)) + j\frac{1}{\sqrt{2}}(1 - 2c(2m + 1)), \quad (1)$$

where j is the imaginary unit, and the pseudo-random sequence $c(i)$ adopts the 31st-order Gold sequence. The generating equation of the initial sequence of $c(i)$ in [23] is

$$c_{\text{init}} = (2^{22} \left\lfloor \frac{n_{\text{ID,seq}}^{\text{PRS}}}{1024} \right\rfloor + 2^{10}(N_{\text{ymb}}^{\text{slot}} n_{s,f}^{\mu} + l + 1) \cdot (2(n_{\text{ID,seq}}^{\text{PRS}} \bmod 1024) + 1) + (n_{\text{ID,seq}}^{\text{PRS}} \bmod 1024)) \bmod 2^{31}, \quad (2)$$

where $n_{\text{ID,seq}}^{\text{PRS}} \in \{0, 1, \dots, 4095\}$ is the downlink PRS sequence ID uniquely identifying a downlink PRS resource, $N_{\text{ymb}}^{\text{slot}}$ is the number of symbols per time slot, $n_{s,f}^{\mu} \in \{0, \dots, N_{\text{slot}}^{\text{frame},\mu} - 1\}$ is the number of time slots within a frame, assuming the subcarrier spacing configuration μ and the number of time slots per frame $N_{\text{slot}}^{\text{frame},\mu}$, and l is the number of OFDM symbols in the time slot to which the sequence is mapped.

Since PRS is generated by the Gold sequence and the Gold sequence has good auto-correlation and cross-correlation characteristics, as shown in Fig. 2, we infer that PRS is suitable for radar sensing.

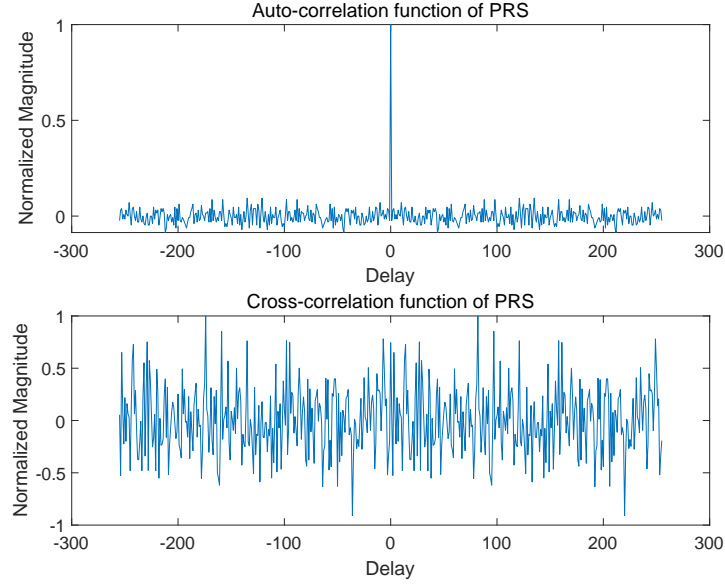


Fig. 2: PRS correlation characteristics

B. Time-Frequency Resource Mapping for PRS

Based on the fact that a physical resource block (PRB) is defined as 12 continuous subcarriers in frequency domain, the PRBs allocated to PRS in TS 38.214 [24] have a granularity of 4 PRBs, a minimum of 24 PRBs and a maximum of 272 PRBs. Table II shows the flexible transmission parameters supported in 5G NR. It is worth mentioning that Δf is the frequency spacing of subcarriers, T_{CP} denotes the length of the cyclic prefix (CP), and T denotes the duration of an OFDM symbol without CP. The 3GPP standard divides the frequencies available to 5G into the Frequency Range 1 (FR1, 450 MHz - 5.9 GHz) band and the Frequency Range 2 (FR2, 24.2 GHz - 52.6 GHz) band.

TABLE II: Flexible transmission parameters supported by 5G NR [23, 25]

μ	0	1	2	3	4
$\Delta f = 2^\mu \cdot 15$ [kHz]	15	30	60	120	240
$N_{\text{slot}}^{\text{slot}}$	14	14	14	14	14
$N_{\text{slot}}^{\text{frame}, \mu}$	10	20	40	80	160
FR1 (450MHz - 5.9GHz)	✓	✓	✓	×	×
FR2 (24.2GHz - 52.6GHz)	×	×	✓	✓	✓
T (μs)	66.67	33.33	16.67	8.33	4.17
T_{CP} (μs)	4.69	2.34	1.17	0.57	0.29
$T+T_{CP}$ (μs)	71.35	35.68	17.84	8.92	4.46

In terms of sequence generation and time-frequency resources, PRS has unique advantages. Consider the downlink reference signals commonly used in 5G NR, namely SS, DMRS and CSI-RS, as comparisons, as shown in Table III. Note that the resource element (RE), defined as an OFDM symbol on a single subcarrier, is the smallest unit of time-frequency resource. SS contains primary synchronization signal (PSS) and secondary synchronization signal (SSS). As shown by Table III, the time-frequency resources of the SS and DMRS are limited. The CSI-RS also occupies fewer time-frequency resources than PRS

due to the multiplexing of different antenna ports, while the PRS is rich in time-frequency resources. Therefore, the performance of PRS based radar sensing is expected to be better.

TABLE III: Comparison of PRS with SS, DMRS and CSI-RS [23, 24]

	SS	DMRS	CSI-RS	PRS
Signal Location	SS is located in the Synchronization Broadcast Block (SSB).	DMRS exists in various physical channels, including downlink and uplink physical channels.	CSI-RS can only be sent on downlink symbols, not on the overlapped PRB with SSB.	The signal dedicated to downlink positioning, which cannot be mapped to the resource particles allocated to the SSB.
Sequence Generation	PSS is a 127-length M sequence, and SSS is a 127-length Gold sequence.	Gold sequence	Gold sequence	Gold sequence with a length of 4096
Time-frequency Resources	PSS and SSS use the first and third symbol in an SSB respectively, occupying 127 subcarriers with the number of sequences from 57 to 183 among 144 REs in the frequency domain.	Front-load DMRS can occupy 1/2 OFDM symbols in the time domain. The DMRS of physical broadcasting channel (PBCH) occupies up to 20 PRBs in the frequency domain.	CSI-RS can support up to 32 different antenna ports, which allows multiplexing in one PRB. The time domain can occupy 1/2/4 OFDM symbols, and the bandwidth can occupy up to 52 PRBs.	The frequency domain has a comb-shaped pilot structure, the bandwidth can occupy a maximum of 272 PRBs, and the time domain can occupy multiple consecutive time slots.

PRS supports flexible time-frequency resource configuration to satisfy the positioning accuracy requirements in different application scenarios and avoid the waste of resources as well. According to the PRS resource mapping scheme defined in TS 38.211, PRS supports four comb forms, namely Comb 2/4/6/12, in the frequency domain, and four symbol number configurations, i.e., Symbol 2/4/6/12, in the time domain.

PRS supports the time-domain patterns summarized in Table IV with the RE offset $k_{\text{offset}}^{\text{PRS}} = 0$, where NA indicates that the mapping mode is not supported. Therefore, the two-dimensional time-frequency

TABLE IV: Time-domain mapping patterns supported by PRS [23]

	2 symbols	4 symbols	6 symbols	12 symbols
Comb 2	0,1	0,1,0,1	0,1,0,1,0,1	0,1,0,1,0,1,0,1,0,1,0,1
Comb 4	NA	0,2,1,3	NA	0,2,1,3,0,2,1,3,0,2,1,3
Comb 6	NA	NA	0,3,1,4,2,5	0,3,1,4,2,5,0,3,1,4,2,5
Comb 12	NA	NA	NA	0,6,3,9,1,7,4,10,2,8,5,11

resource mapping diagrams of PRS in one time slot (14 OFDM symbols) and 12 consecutive subcarriers (one PRB) are obtained, as shown in Fig. 3.

It can be summarized that the time-frequency resource allocation for PRS is flexible, so that multiple different downlink PRS signals from multiple base stations are multiplexed on different subcarriers in a comb-like manner. Thus, the comb structure of PRS is to control the interference of PRS signals transmitted by multiple BSs. For the radar sensing using PRS, it is also necessary to distinguish signals through different time-frequency structures to reduce interference.

III. JSC SIGNAL MODEL

In this section, the PRS based JSC signal model is proposed. We consider the scenario where the 5G BS sends the downlink PRS to the target, and uses the echo signal from the target for range and velocity estimation. In addition, the ambiguity function is derived to further demonstrate its feasibility in radar sensing.

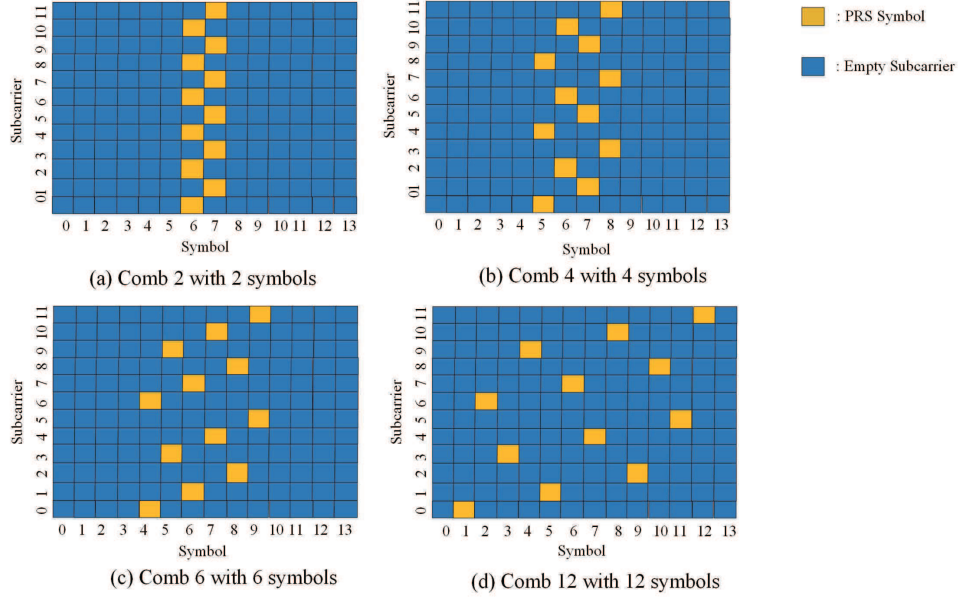


Fig. 3: The two-dimensional time-frequency resource map ping diagrams for PRS

A. Signal Model of PRS

Taking Comb 4 with 4 symbols as an example, the PRS mapped OFDM signal model is shown in Fig. 4. In a time slot, PRS occupies M OFDM symbols in the time domain, N subcarriers in the frequency domain, and the number of subcarriers carrying PRS is N_J ($N/K_{\text{comb}}^{\text{PRS}}$), where J is the set of subcarriers carrying PRS.

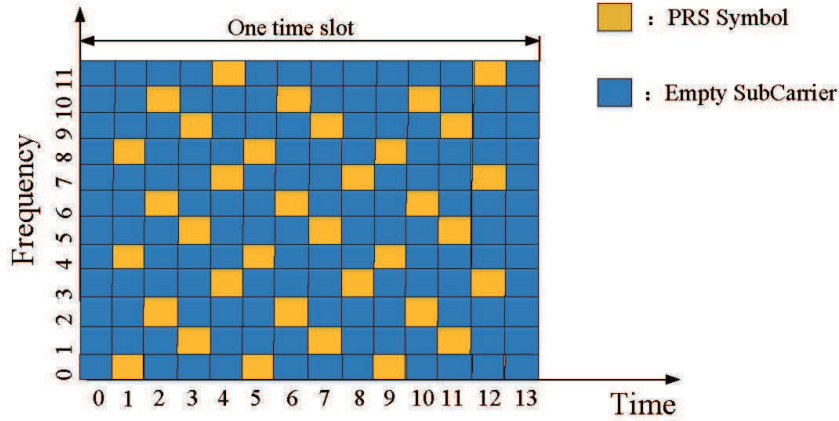


Fig. 4: PRS mapped OFDM signal model

The continuous time domain signal expression is

$$x(t) = \sum_{m=0}^{M-1} \sum_{k=0}^{N_J-1} s(k, m) \times e^{j2\pi f_k t} \text{rect}\left(\frac{t - mT_s}{T_s}\right), \quad (3)$$

where $s(k, m)$ represents the modulated PRS symbol, with subcarrier index k and OFDM symbol index m . T_s is the total duration of the OFDM symbol which satisfies $T_s = T + T_{\text{CP}}$. $\Delta f = 1/T$ is the frequency spacing of subcarriers, f_k is the frequency of the k -th subcarriers that carry the PRS symbol. $\text{rect}(t/T_s)$ is the rectangular function, which is equal to 1, for $0 \leq t < T_s$, and 0, otherwise.

With the PRS equally spaced in frequency domain, the frequency of the subcarriers carrying PRS symbols f_k satisfies the following equation.

$$f_k = (K_{\text{comb}}^{\text{PRS}} \times k + k_0)\Delta f \quad k = 0, \dots, N_J - 1, \quad (4)$$

where $K_{\text{comb}}^{\text{PRS}}$ is the comb size of PRS, k_0 is the index of the first subcarrier carrying PRS, which is related to m and $K_{\text{comb}}^{\text{PRS}}$.

Taking Comb 4 with 4 symbols as an example, $K_{\text{comb}}^{\text{PRS}} = 4$, and k_0 can take 0, 2, 1, 3 in turn. The relation between k_0 and m is shown in (5)

$$k_0 = \frac{m \bmod K_{\text{comb}}^{\text{PRS}}}{2} + \frac{3}{4} \left[1 - (-1)^{m \bmod K_{\text{comb}}^{\text{PRS}}} \right], \quad (5)$$

where mod refers to a modulo operation.

B. Received Radar Signal

According to radar signal processing algorithm in [10], the echo signal received by radar receiver is

$$S_{\text{Rx}}[k, m] = \xi S_{\text{Tx}}[k, m] \times e^{-j2\pi(K_{\text{comb}}^{\text{PRS}}k\Delta f)\frac{2R_r}{c}} \times e^{j2\pi(K_{\text{comb}}^{\text{PRS}}mT_s)f_{d,r}}, \quad (6)$$

where $S_{\text{Tx}}[k, m]$, $S_{\text{Rx}}[k, m]$ are the transmitted and the received modulation symbols respectively, ξ is the attenuation factor, which is regarded as constant during the transmission of PRS. R_r is the range of target, $f_{d,r}$ is the Doppler shift, and c is the speed of light.

Dividing the received modulation symbols $S_{\text{Rx}}[k, m]$ by the transmitted modulation symbols $S_{\text{Tx}}[k, m]$, the following matrix $(S_g)_{k,m}$ is obtained.

$$(S_g)_{k,m} = \frac{S_{\text{Rx}}[k, m]}{S_{\text{Tx}}[k, m]} = \xi (\bar{k}_r \otimes \bar{k}_d), \quad (7)$$

where $\bar{k}_r(k) = e^{-j2\pi(K_{\text{comb}}^{\text{PRS}}k\Delta f)\frac{2R_r}{c}}$ and $\bar{k}_d(m) = e^{j2\pi(K_{\text{comb}}^{\text{PRS}}mT_s)f_{d,r}}$ are the two vectors carrying the range and the Doppler information. \otimes refers to a dyadic product.

C. Ambiguity Function of PRS

The definition of ambiguity function is

$$\chi(\tau, f_{d,r}) = \int_{-\infty}^{\infty} x(t)x^*(t-\tau) e^{j2\pi f_{d,r}t} dt, \quad (8)$$

where $x^*(\cdot)$ is a conjugate operation, τ is the round-trip delay experienced by signal transmission.

Substituting the signal expression of (3) into (8), the following expression can be obtained.

$$\begin{aligned} \chi(\tau, f_{d,r}) &= \sum_{m_1=0}^{M-1} \sum_{m_2=0}^{M-1} \sum_{k_1=0}^{N_J-1} \sum_{k_2=0}^{N_J-1} s(k_1, m_1) s^*(k_2, m_2) \\ &\cdot e^{j2\pi f_{k_2}\tau} \cdot \int_{-\infty}^{+\infty} e^{j2\pi(f_{k_1}-f_{k_2}+f_{d,r})t} \text{rect}\left(\frac{t-m_1T_s}{T_s}\right) \\ &\times \text{rect}\left(\frac{t-\tau-m_2T_s}{T_s}\right) dt \end{aligned} \quad (9)$$

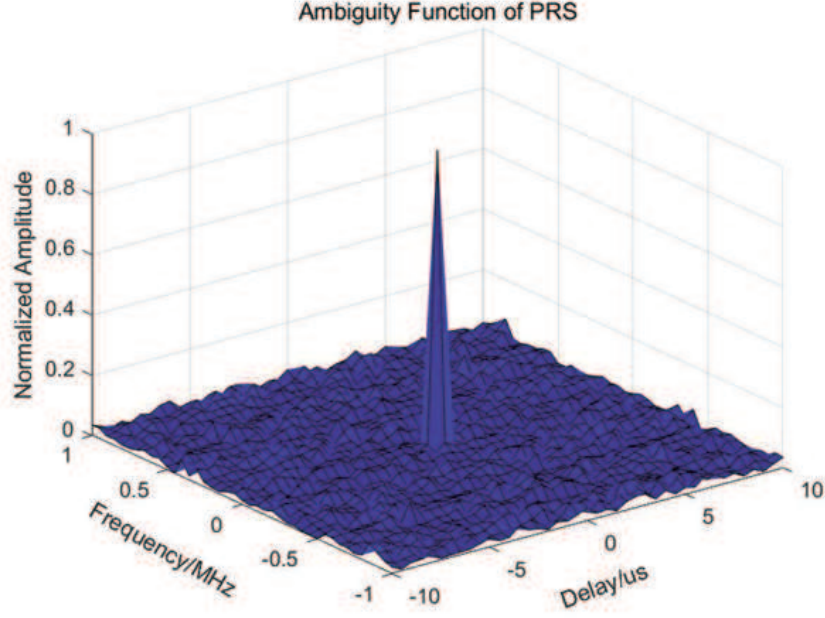


Fig. 5: Ambiguity function of PRS (Comb 4 with 4 symbols, $N=1024$, $N_J=256$)

The ambiguity function of PRS can be abbreviated as

$$\begin{aligned}
 \chi(\tau, f_{d,r}) &= \sum_{m_1=0}^{M-1} \sum_{m_2=0}^{M-1} \sum_{k_1=0}^{N_J-1} \sum_{k_2=0}^{N_J-1} s(k_1, m_1) s^*(k_2, m_2) \\
 &\cdot e^{j2\pi f_{k_2} \tau} \int_{t_{\min}}^{t_{\max}} e^{j2\pi(f_{k_1} - f_{k_2} + f_{d,r})t} dt \\
 &= t_{\max - \min} \sum_{m_1=0}^{M-1} \sum_{m_2=0}^{M-1} \sum_{k_1=0}^{N_J-1} \sum_{k_2=0}^{N_J-1} s(k_1, m_1) s^*(k_2, m_2) \\
 &\cdot e^{j2\pi f_{k_2} \tau} \cdot \text{sinc}((f_{k_1} - f_{k_2} + f_{d,r}) t_{\max - \min}) \\
 &\cdot e^{j2\pi(f_{k_1} - f_{k_2} + f_{d,r}) t_{\text{avg}}}
 \end{aligned} \tag{10}$$

where $\text{sinc}(\cdot)$ refers to a normalized sinc function, the definitions of t_{\max} , t_{\min} , $t_{\max - \min}$ and t_{avg} are as follows.

$$\begin{aligned}
 t_{\max} &= \min \{(m_1 + 1) T_s, \tau + (m_2 + 1) T_s\}, \\
 t_{\min} &= \max \{m_1 T_s, \tau + m_2 T_s\}, \\
 t_{\max - \min} &= t_{\max} - t_{\min}, \\
 t_{\text{avg}} &= \frac{t_{\max} + t_{\min}}{2}.
 \end{aligned} \tag{11}$$

It can be discovered from Fig. 5 that the ambiguity function of PRS is “pushpin type” which can provide high range and velocity resolution at the same time. Thus, PRS has the potential to realize radar sensing.

IV. PRS BASED RADAR SENSING

In this section, the radar signal processing algorithm in [10] is adopted. Then, the resolution, the maximum unambiguous range/velocity, and the accuracy of PRS based radar sensing are analyzed. Besides, the methods improving the accuracy of radar sensing are proposed.

A. Range Estimation using PRS

N_J -point inverse fast Fourier transform (IFFT) is performed on the PRS, which is inserted at equal intervals in the frequency domain. IFFT is performed on the m -th column of the $(S_g)_{k,m}$

$$r(l) = \text{IFFT}(S_{g,m}(k)) = \sum_{k=0}^{N_J-1} e^{-j2\pi K_{\text{comb}}^{\text{PRS}} \Delta f k \frac{2R_r}{c}} \times e^{j2\pi lk/N_J} \quad (12)$$

$$l \in \{0, 1, \dots, N_J - 1\},$$

where $\text{IFFT}(\cdot)$ is a inverse fast Fourier transform operation. l is the index of the l -th result of N_J -point IFFT. The peak occurs when the two exponential terms in (12) cancel each other. With the index of the peak of column m recorded as $\text{ind}_{S_{g,m}}$, the estimated range \hat{R}_r is derived as

$$\begin{aligned} \hat{R}_r &= \frac{c}{2N_J K_{\text{comb}}^{\text{PRS}} \Delta f} \\ &= \frac{\text{ind}_{S_{g,m}} c}{2N \Delta f} \quad \text{ind}_{S_{g,m}} \in \{0, 1, \dots, N_J - 1\}. \end{aligned} \quad (13)$$

The range resolution ΔR is derived as

$$\Delta R = \frac{c}{2N \Delta f}. \quad (14)$$

Limited by the maximum value of $\text{ind}_{S_{g,m}}$, the maximum unambiguous range R_{max} can be expressed as (15)

$$R_{\text{max}} = \frac{N_J c}{2N \Delta f} = \frac{c}{2K_{\text{comb}}^{\text{PRS}} \Delta f}. \quad (15)$$

(15) shows that short-range, medium-range, and long-range ranging can be realized by tuning the comb size of PRS $K_{\text{comb}}^{\text{PRS}}$. However, the restriction imposed by the guard interval is usually more stringent in actual target detection.

Averaging the estimated results of all columns of $(S_g)_{k,m}$ yields an estimate of the range \hat{R}_r . With N_t measurements, the root mean square error (RMSE) of the range estimation is derived as

$$\text{RMSE}(R_r) = \sqrt{\frac{1}{N_t} \sum_{i=1}^{N_t} (\hat{R}_r[i] - R_r)^2}. \quad (16)$$

According to [22], the method of increasing the number of IFFT points can be adopted to improve the ranging accuracy. By introducing the fractional factor m_a , the estimation function using fractional Fourier transform (FRFT) is

$$\begin{aligned} \text{IFFT}(S_{g,m}(k)) &= \frac{1}{m_a \times N_J} \sum_{k=0}^{m_a \times N_J - 1} e^{-j2\pi K_{\text{comb}}^{\text{PRS}} \Delta f k \frac{2R_r}{c}} \\ &\times e^{\frac{j2\pi lk}{m_a \times N_J}}. \end{aligned} \quad (17)$$

Meanwhile, the range estimation in (13) can be rewritten as

$$\hat{R}_{r,m_a} = \frac{\text{ind}_{S_{g,m}}^{m_a} c}{2 \times m_a \times N \Delta f} \quad \text{ind}_{S_{g,m}}^{m_a} \in \{0, 1, \dots, m_a \times N_J - 1\}, \quad (18)$$

where $\text{ind}_{S_{g,m}}^{m_a}$ is the index of the peak for IFFT after introducing the fractional factor m_a .

The fractional factor increases more search steps. Due to the fine accuracy of the estimation curve, the ranging accuracy is improved [22]. However, the ranging accuracy will only approach CRLB with infinitely increasing m_a . Since the complexity of IFFT is $o(m_a \times N \cdot \log_2(m_a N))$, the tradeoff between accuracy and complexity when choosing m_a needs to be considered. However, the maximum unambiguous range does not change with the increase of the IFFT points.



Fig. 6: Velocity measurement using multiple frames (Pre is the abbreviation of preamble sequence)

B. Velocity Estimation using PRS

Similar to the range estimation, M_J ($M/K_{\text{comb}}^{\text{PRS}}$)-points fast Fourier transform (FFT) is performed on the M_J PRS symbols, which is inserted at equal intervals in the time domain. FFT is performed on the k -th row of the $(S_g)_{k,m}$

$$v(d) = \text{FFT}(S_{g,k}(m)) = \sum_{m=0}^{M_J-1} e^{j2\pi(K_{\text{comb}}^{\text{PRS}}mT_s)f_{d,r}} \times e^{-j2\pi dm/M_J} \quad d \in \{0, 1, \dots, M_J - 1\}, \quad (19)$$

where $\text{FFT}(\cdot)$ is a fast Fourier transform operation. d is the index of the d -th result of M_J -point FFT. Recording the peak index of row k as $\text{ind}_{S_g,k}$, the estimation of Doppler frequency shift $\hat{f}_{d,r}$ is:

$$\hat{f}_{d,r} = \frac{\text{ind}_{S_g,k}}{MT_s}. \quad (20)$$

According to the relation between velocity v and Doppler frequency shift $\hat{f}_{d,r}$

$$v = \frac{cf_{d,r}}{2f_c}, \quad (21)$$

where f_c is the carrier frequency of the transmitted signal, the estimation of velocity \hat{v} is

$$\hat{v} = \frac{\text{ind}_{S_g,k}c}{2MT_s f_c} \quad \text{ind}_{S_g,k} \in \{0, 1, \dots, M_J - 1\}. \quad (22)$$

The velocity resolution Δv is shown in (23).

$$\Delta v = \frac{c}{2MT_s f_c}, \quad (23)$$

and the maximum unambiguous velocity v_{max} is

$$v_{\text{max}} = \frac{M_J c}{2MT_s f_c} = \frac{c}{2K_{\text{comb}}^{\text{PRS}} T_s f_c}. \quad (24)$$

All rows are averaged to provide an estimate of velocity \hat{v} . The RMSE of the velocity estimation is

$$\text{RMSE}(v) = \sqrt{\frac{1}{N_t} \sum_{i=1}^{N_t} (\hat{v}[i] - v)^2}. \quad (25)$$

The method of increasing the number of FFT points can also be adopted to improve the accuracy of velocity measurement, thereby reducing the number of PRS symbols and the overhead of the required time slot. The maximum unambiguous velocity does not change with the increase of the FFT points.

However, the increase of FFT points will bring computational complexity. And the velocity measurement using single frame will consume too many time slots within a frame. Thus, the velocity measurement using multiple frames is proposed to reduce the overhead in each frame. The details are shown in Fig. 6.

N_f 5G downlink frames are continuously sent. The time domain resources occupied by PRS in the i -th downlink frame contain S_i ($i=1, 2, \dots, N_f$) symbols. The receiver extracts the PRS symbols in each frame for velocity estimation

$$\text{FFT}(S_{g,k}(m)) = \sum_{m=0}^{S_J-1} e^{j2\pi(K_{\text{comb}}^{\text{PRS}}mT_s)f_{d,r}} \times e^{-j2\pi dm/S_J}, \quad (26)$$

where $S_J = \sum_{i=1}^{N_f} S_i / K_{\text{comb}}^{\text{PRS}}$ is the PRS symbols inserted at equal intervals in the time domain which are extracted from N_f frames.

The estimation of velocity \hat{v}_{multi} is

$$\hat{v}_{\text{multi}} = \frac{\text{ind}_{S_g, k}^{\text{multi}} c}{2T_s f_c (\sum_{i=1}^{N_f} S_i)}, \quad (27)$$

$$\text{ind}_{S_g, k}^{\text{multi}} \in \{0, 1, \dots, S_J - 1\}$$

where $\text{ind}_{S_g, k}^{\text{multi}}$ is the peak index of velocity measurement using multiple frames.

The velocity resolution Δv_{multi} is derived as

$$\Delta v_{\text{multi}} = \frac{c}{2T_s f_c (\sum_{i=1}^{N_f} S_i)}. \quad (28)$$

PRS symbol overhead η_i in the i -th frame is defined as

$$\eta_i = \frac{S_i}{N_{\text{slot}}^{\text{frame}, \mu} \cdot N_{\text{symp}}^{\text{slot}}}. \quad (29)$$

In addition, we define the sensing refresh time ρ to represent the time to achieve a velocity measurement

$$\rho = N_f \cdot T_f, \quad (30)$$

where $T_f = 10$ ms is the duration of per frame.

For the velocity measurement using multiple frames, the total number of PRS symbols used for sensing is increased compared with a single frame, thereby improving the velocity resolution Δv_{multi} . Thus, the accuracy of velocity estimation is improved. Besides, the overhead within a frame η_i is reduced, with the cost of increasing the sensing refresh time ρ which indicates the time to achieve a velocity measurement becomes longer.

Referring to the scenario of JSC roadside BS detecting vehicles shown in Fig. 1, the long sensing refresh time means that the vehicle has to travel a long range to achieve a velocity measurement, which may cause the vehicle velocity to change during this period, namely, the velocity estimation is not updated in time. Therefore, there is a performance tradeoff among the velocity resolution Δv_{multi} , overhead in the i -th frame η_i and sensing refresh time ρ .

In addition, PRS is sent in the 5G downlink frame for sensing, so that sensing and communication functions are time-division multiplexed. The impact of velocity measurement using multiple frames on communication performance is mainly reflected in the symbol overhead. Assuming that M_d data symbols are transmitted in a single frame and P -QAM modulation is adopted, the maximum communication data rate R_d of a single frame is

$$R_d = M_d \times N \times \log_2 P / T_f, \quad (31)$$

The reduction of PRS symbol overhead η_i indicates that the amount of resources used for communication in a frame increases, which improves the communication rate.

V. CRLB OF RADAR SENSING AND POSITIONING

In this section, we derive the CRLBs of PRS based radar sensing and positioning.

A. CRLB of PRS based Radar Sensing

Theorem 1. When $M \gg 1, N \gg 1$, the CRLB of the range and velocity estimated by the PRS based radar sensing is

$$CRLB(R_r) = \frac{c^2 T^2}{\xi^2 SNR (2\pi)^2} \frac{12}{MN(N_J - 1)(7N_J + 1)}, \quad (32)$$

$$CRLB(v) = \frac{c^2}{\xi^2 SNR (2\pi)^2 f_c^2 T_s^2} \frac{12}{NM(M_J - 1)(7M_J + 1)}, \quad (33)$$

where SNR is signal-to-noise ratio.

Proof. For the traditional OFDM system, since the radar receiver has known modulation symbols and the noise obeys one-dimensional Gaussian distribution, the radar observations after phase-by-phase rotation [26] are expressed as

$$z_{m,n} = \xi A_{m,n} e^{j2\pi K_{\text{comb}}^{\text{PRS}} m T_s f_{d,r}} e^{-j2\pi n K_{\text{comb}}^{\text{PRS}} \Delta f \tau} + w_{m,n}, \quad (34)$$

where $A_{m,n} = |x_{m,n}|$ is the amplitude of the transmitted symbol. $w_{m,n}$ is the additive white Gaussian noise (AWGN) with σ^2 variance and zero mean.

The received signal with unknown parameter $\theta = (\tau, f_{d,r})$ is observed, then the likelihood function is

$$f(z|\tau, f_{d,r}) = \frac{1}{(2\pi\sigma^2)^{\frac{MN}{2}}} e^{-\frac{1}{2\sigma^2} \sum_m \sum_n \left| z_{m,n} - \xi A_{m,n} e^{j2\pi K_{\text{comb}}^{\text{PRS}} m T_s f_{d,r}} e^{-j2\pi n K_{\text{comb}}^{\text{PRS}} \Delta f \tau} \right|^2}. \quad (35)$$

The log likelihood function $L(z|\tau, f_{d,r})$ is derived as

$$L(z|\tau, f_{d,r}) = \ln f(z|\tau, f_{d,r}) = -\frac{MN}{2} \ln(2\pi\sigma^2) - \frac{1}{2\sigma^2} \sum_m \sum_n \left| z_{m,n} - \xi A_{m,n} e^{j2\pi K_{\text{comb}}^{\text{PRS}} m T_s f_{d,r}} e^{-j2\pi n K_{\text{comb}}^{\text{PRS}} \Delta f \tau} \right|^2, \quad (36)$$

with $s_{m,n} = \xi A_{m,n} e^{j2\pi K_{\text{comb}}^{\text{PRS}} m T_s f_{d,r}} e^{-j2\pi n K_{\text{comb}}^{\text{PRS}} \Delta f \tau}$. (35) can be simplified as

$$L(z|\tau, f_{d,r}) = -\frac{MN}{2} \ln(2\pi\sigma^2) - \frac{1}{2\sigma^2} \sum_m \sum_n |z_{m,n} - s_{m,n}|^2. \quad (37)$$

Further, we can obtain the second-order Fisher information matrix F as follows.

$$\begin{aligned} F &= \begin{bmatrix} F_{\tau\tau} & F_{\tau f_{d,r}} \\ F_{f_{d,r}\tau} & F_{f_{d,r}f_{d,r}} \end{bmatrix} \\ &= - \begin{bmatrix} E\left(\frac{\partial^2 L}{\partial \tau^2}\right) & E\left(\frac{\partial^2 L}{\partial \tau \partial f_{d,r}}\right) \\ E\left(\frac{\partial^2 L}{\partial f_{d,r} \partial \tau}\right) & E\left(\frac{\partial^2 L}{\partial f_{d,r}^2}\right) \end{bmatrix} \\ &= \frac{1}{\sigma^2} \left(\sum_m \sum_n \left[\frac{\partial s_{m,n}}{\partial \theta_i} \cdot \frac{\partial s_{m,n}^*}{\partial \theta_j} \right]_{ij} \right). \end{aligned} \quad (38)$$

The CRLB matrix for time delay and Doppler shift estimation is the inverse of the Fisher information matrix as follows.

$$\begin{bmatrix} CRLB(\tau) & CRLB(\tau, f_{d,r}) \\ CRLB(f_{d,r}, \tau) & CRLB(f_{d,r}) \end{bmatrix} = F^{-1}. \quad (39)$$

Assuming $M \gg 1, N \gg 1$, the CRLB of range and velocity can be obtained.

$$\begin{aligned} CRLB(\tau) &= \frac{F_{f_{d,r}f_{d,r}}}{F_{\tau\tau}F_{f_{d,r}f_{d,r}} - F_{\tau f_{d,r}}F_{f_{d,r}\tau}} \\ &= \frac{T^2}{\xi^2 SNR (2\pi)^2} \cdot \frac{48}{MN(N_J - 1)(7N_J + 1)}, \end{aligned} \quad (40)$$

$$\begin{aligned}
CRLB(f_{d,r}) &= \frac{F_{\tau\tau}}{F_{\tau\tau}F_{f_{d,r}f_{d,r}} - F_{\tau f_{d,r}}F_{f_{d,r}\tau}} \\
&= \frac{1}{\xi^2 SNR \cdot (2\pi)^2 \cdot T_s^2} \cdot \frac{48}{NM(M_J-1)(7M_J+1)}.
\end{aligned} \tag{41}$$

According to the relation $R_r = c\tau/2$ and (21), (31) and (32) can be derived based on the following relation

$$CRLB(R_r) = \frac{c^2}{4} CRLB(\tau), \tag{42}$$

$$CRLB(v) = \frac{c^2}{4f_c^2} CRLB(f_{d,r}). \tag{43}$$

□

(32-33) show that with the decreasing of T , the CRLB of range estimation decreases, while the CRLB of velocity estimation increases. There is a performance tradeoff between range and velocity estimation. Therefore, the parameters can be reasonably configured to satisfy the accuracy requirements for range and velocity estimation in actual radar sensing.

B. CRLB of PRS based Positioning

Theorem 2. *The CRLB for PRS positioning is*

$$CRLB(R_r) = \frac{c^2 T^2}{\frac{4\pi^2}{3} \cdot SNR \cdot N(N_J - 1)(2N_J - 1)}. \tag{44}$$

Proof. The BS generates the PRS according to the high-level parameter configuration, and maps the PRS to the physical resource unit, and finally obtains the OFDM baseband signal $x[n]$ using one symbol through IFFT.

$$\begin{aligned}
x[n] &= \sqrt{\frac{C}{N}} \sum_{l \in J} p_l \cdot s_l \cdot e^{j2\pi nl} \\
&= \sqrt{\frac{C}{N}} e^{j2\pi nk_0} \sum_{k=0}^{N_J-1} p_k \cdot s_k \cdot e^{j2\pi nk/N_J},
\end{aligned} \tag{45}$$

where C is the signal power, and s_k is the PRS. k_0 is the index of the first subcarrier carrying PRS given in (4). p_k^2 is the relative power weight of subcarrier k with $\sum_k p_k^2 = N$. Assuming that the power is evenly distributed on all subcarriers carrying PRS, the relative power weight of subcarrier k is

$$p_k = \sqrt{\frac{N}{N_J}} = \sqrt{K_{\text{comb}}^{\text{PRS}}}, \quad k \in J. \tag{46}$$

Therefore, according to general CRLB derivation results of signals in gaussian white noise given by Kay [27] and the derivation in [28], the CRLB estimation of the delay for PRS positioning is

$$CRLB(\tau) = \frac{T^2}{\frac{4\pi^2}{3} \cdot SNR \cdot N(N_J - 1)(2N_J - 1)}. \tag{47}$$

Thus, the range estimation of CRLB in (44) can be obtained. □

VI. SIMULATIONS AND NUMERICAL RESULTS

In this section, we first provide simulation results of radar signal processing method to verify the feasibility of PRS based radar sensing in range and velocity estimation. Then, the performance of range and velocity estimation is provided and compared with CRLB. In addition, we give some suggestions for the frame structure design for 5G-A and 6G.

TABLE V: simulation parameters [23]

Symbol	Parameter	Value
f_c	Carrier frequency	24 GHz
Δf	Frequency spacing of subcarriers	120 kHz
T_s	Total duration of OFDM symbol	8.92 μs
N	Number of subcarriers	256
$K_{\text{comb}}^{\text{PRS}}$	Comb size of PRS	4/2
N_J ($N/K_{\text{comb}}^{\text{PRS}}$)	Number of subcarriers carrying PRS	64/128
R_r	Range of target	50 m
v	Velocity of target	15 m/s

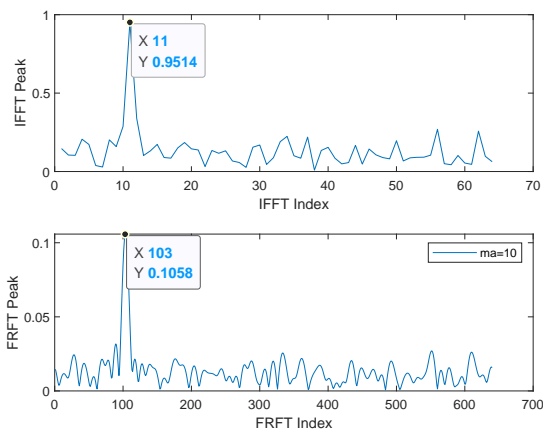


Fig. 7: Simulated IFFT correlation peak when the target is at 50 m

A. Range Estimation

For the OFDM waveform modulated by PRS sequence, one time slot accounts for up to 12 symbols. The SNR is 5 dB. The rest of simulation parameters are shown in Table V.

A measurement result is shown in Fig. 7, where the theoretical value of range resolution is $\Delta R = \frac{c}{2N\Delta f} = 4.88$ m. Since the peak index of column IFFT in Fig. 7 is 11 and the count starts from 1 in the simulation, the value of $ind_{S_g,m}$ is 10. The estimated range is

$$\hat{R}_r = \frac{ind_{S_g,m}c}{2N\Delta f} = 48.83 \text{ m.} \quad (48)$$

With the fractional factor $m_a = 10$, the value of $ind_{S_g,m}^{m_a}$ is 102 and the estimated range is

$$\hat{R}_{r,m_a} = \frac{ind_{S_g,m}^{m_a}c}{2 \times m_a \times N\Delta f} = 49.80 \text{ m.} \quad (49)$$

With 1000 times Monte Carlo simulations, the RMSE of range estimation is 1.17 m. When introducing the fractional factor, the RMSE is reduced to 0.33 m. From the results of range estimation, the ranging accuracy is significantly improved and reached the centimeter level.

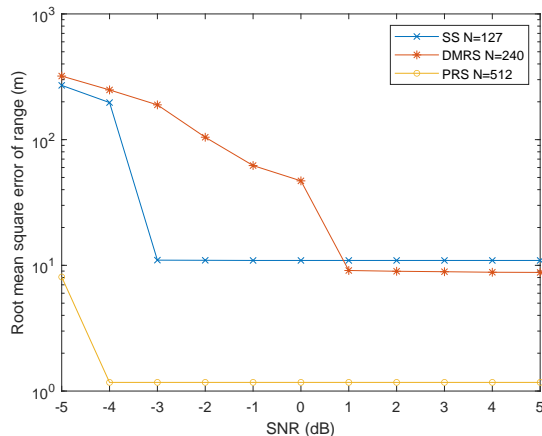


Fig. 8: Comparison of RMSEs of range estimations between SS and PRS

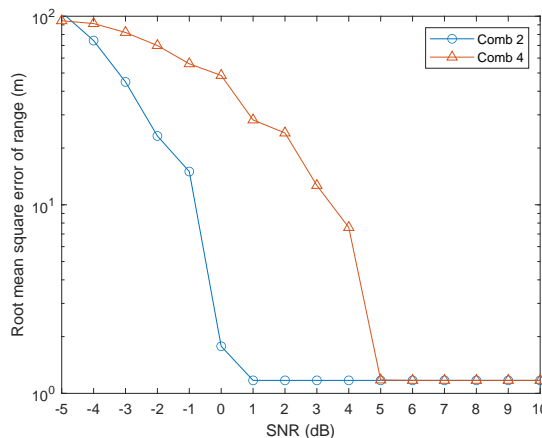


Fig. 9: Comparison of RMSEs of range estimations between Comb 2 and Comb 4

Since the CSI-RS occupies very few REs in one PRB due to the multiplexing of different antenna ports, we only compare the RMSE of range estimation among SS, DMRS and PRS to illustrate the feasibility of PRS for radar sensing, as shown in Fig. 8. The ranging accuracy of the radar signal processing algorithm in this paper is limited by the number of subcarriers. Therefore, the comparison of the sensing performance of different reference signals essentially lies in their different time-frequency resources. The comb of PBCH DMRS in the frequency domain, occupies up to 240 consecutive subcarriers. For a reasonable comparison, the length of PRS sequence is set the same as the synchronization sequence and the comb size is 4 in Fig. 8. Since the frequency domain is comb-shaped, PRS occupies more frequency resources than SS. Hence, the ranging performance of PRS is significantly better than that of SS. Although both PRS and DMRS are mapped with Comb 4 in the frequency domain, the PRS sequence is longer, so the ranging accuracy is better. The result shows that PRS is suitable for radar sensing.

Fig. 9 shows that the comb form of PRS also affects the ranging accuracy. It is worth mentioning that the RMSEs of range become unchangeable when SNR reaches a certain threshold in Fig. 8 and Fig. 9, it is comprehensible according to the estimated range given in (13). The (13) shows that since the peak index $ind_{S_g,m}$ can only be taken as an integer, there will be a minimum error between the estimated range and the real range. With the increase of SNR, The RMSEs of range gradually converges to the minimum error and will not change, which is the best accuracy that can be achieved under high SNR caused by the resolution of algorithm. With the increase of SNR, the RMSE of Comb 2 converges faster. In the case of low SNR, the ranging accuracy of Comb 2 is better than that of Comb 4. The reason is

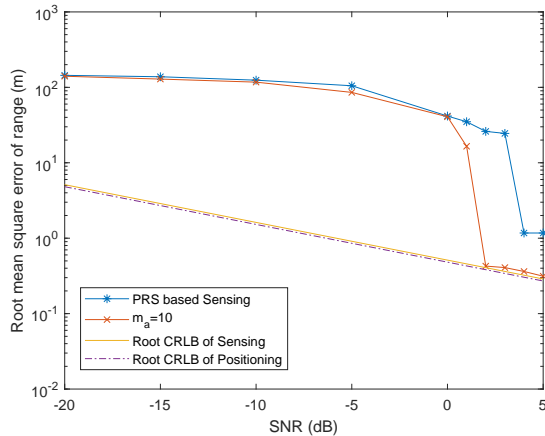


Fig. 10: RMSEs of range estimations vs SNR

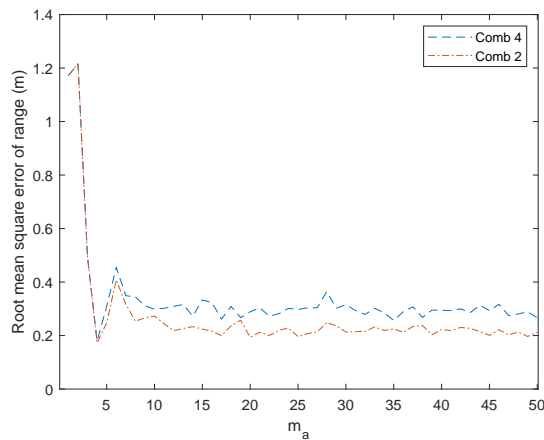


Fig. 11: RMSEs of range estimations vs m_a

that Comb 4 inserts fewer subcarriers so that it has a smaller peak value, which is more susceptible to noise. Comb 2 performs better in the links with low and medium SNRs, but its performance advantage gradually decreases with the improvement of SNR. In the scenarios with small delay spread, especially in the area of high SNR, Comb 4 with lower overhead has higher throughput performance.

Fig. 10 shows that the RMSE of the range estimation and the root CRLB of the range estimation decrease with the increase of SNR, and the RMSE of the range estimation gradually approaches the root CRLB. When introducing the fractional factor m_a , the curve converges faster and approaches the CRLB. Fig. 11 shows the impact of different values of m_a on the improvement of RMSE. Considering the tradeoff between accuracy requirements and complexity, the appropriate value of m_a is greater than 10.

B. Velocity Estimation

Supposing that PRS is sent continuously, and the number of symbols is $M = 128$. For one measurement result as shown in Fig. 12, the theoretical value of velocity resolution $\Delta v = \frac{c}{2MT_s f_c} = 5.47$ m/s and the value of $ind_{S_g, k}$ is 3. Thus, the estimated velocity is

$$\hat{v} = \frac{ind_{S_g, k} c}{2MT_s f_c} = 16.42 \text{ m/s.} \quad (50)$$

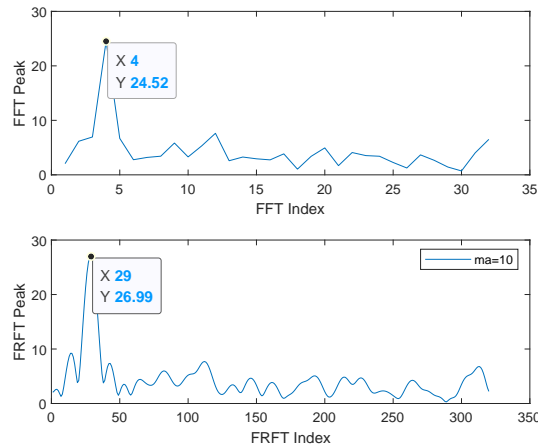


Fig. 12: Simulated FFT correlation peak when the target's velocity is 15 m/s

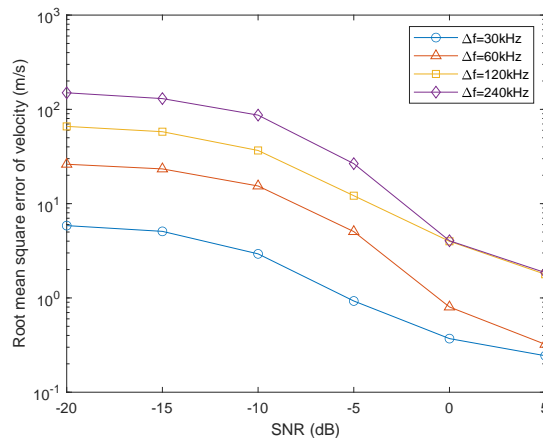


Fig. 13: Comparison of RMSEs of velocity estimations with different subcarrier intervals

Taking the fractional factor $m_a = 10$, the peak index $ind_{S_g,k}^{m_a}$ for FFT after introducing m_a is 28, the estimated velocity is

$$\hat{v}_{m_a} = \frac{ind_{S_g,k}^{m_a} c}{2m_a \times MT_s f_c} = 15.33 \text{ m/s}. \quad (51)$$

After 1000 times Monte Carlo simulations, the RMSE of velocity estimation is 2.24 m/s. When introducing the fractional factor, the value of RMSE is reduced to 0.69 m/s. It is revealed that the introduction of fractional factor improves the accuracy of velocity estimation, which reaches the cm/s level.

Fig. 13 shows that the RMSE of velocity estimation decreases with the increase of SNR, and the subcarrier spacing also affects the accuracy of velocity estimation. The accuracy of velocity estimation is increasing with the decrease of the subcarrier spacing. The accuracy of velocity estimation is increasing with the decrease of Δf . Although the resolution at 120 kHz is 2 times higher than that at 240 kHz, the resolution is still very poor, and the improvement of accuracy is not obvious.

RMSEs of velocity estimations vs SNR are shown in Fig. 14. The RMSE and the root CRLB of the velocity estimation decrease as the SNR increases. With the introduction of the fractional factor, the RMSE curve of the velocity estimation converges faster.

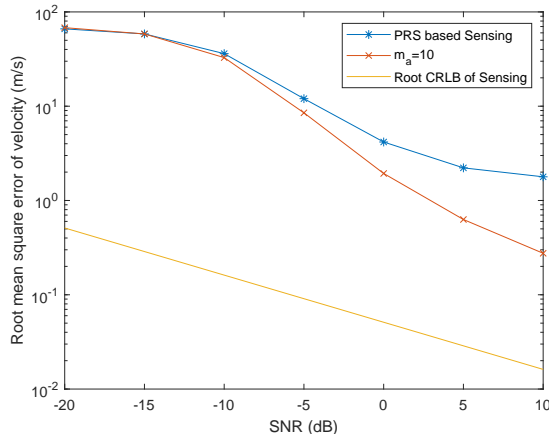


Fig. 14: RMSEs of velocity estimations vs SNR

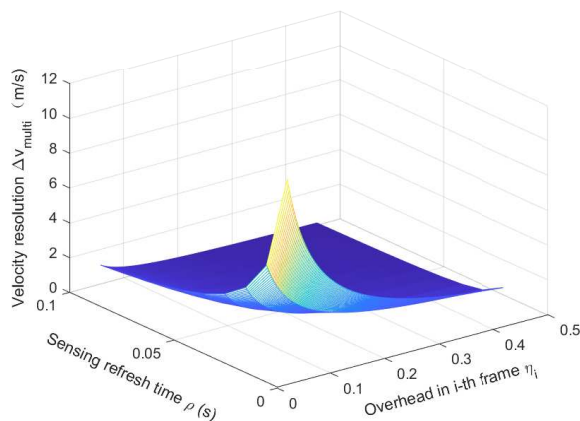


Fig. 15: Relationship among velocity resolution Δv_{multi} , overhead in i -th frame η_i and sensing refresh time ρ

C. Velocity Measurement using Multiple Frames

Taking $\Delta f = 60\text{kHz}$, then a 5G NR frame has 560 symbols. Assuming that the number of symbols occupied by PRS per frame S_i is 128, and the rest symbols are filled with random data modulated by QPSK.

Fig. 15 shows the relationship among velocity resolution Δv_{multi} , overhead in i -th frame η_i and sensing refresh time ρ . The velocity resolution Δv_{multi} can be improved by increasing the PRS symbol overhead in a single frame η_i or increasing the sensing refresh time ρ . To ensure high velocity resolution, η_i is reduced by sacrificing the sensing refresh time ρ , namely, using more frames for velocity measurement.

Fig. 16 shows the performance of velocity measurement using multiple frames with different SNRs. When the number of frames is the same, the RMSE of velocity measurement decreases with the increase of SNR, improving the anti-noise performance. With the increase of the number of frames, the accuracy of velocity estimation is improved. Since S_i is 128, the PRS symbol overhead η_i in a single frame is 22.9%. In order to ensure the accuracy of velocity measurement, assuming that three frames are used for velocity measurement, the sensing refresh time ρ is 0.03 s so that the vehicle travels 0.45 m during velocity estimation with the velocity of 54 km/h, which is tolerable.

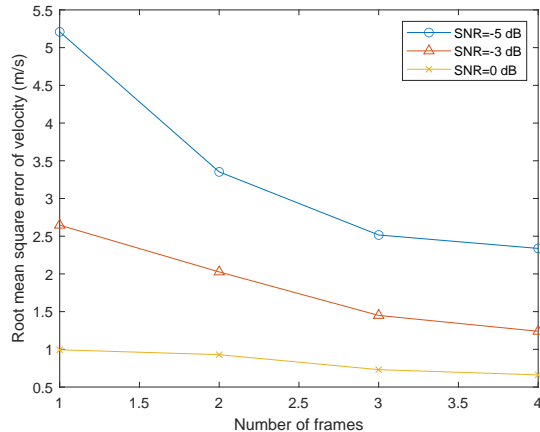


Fig. 16: RMSEs of velocity estimations vs number of frames

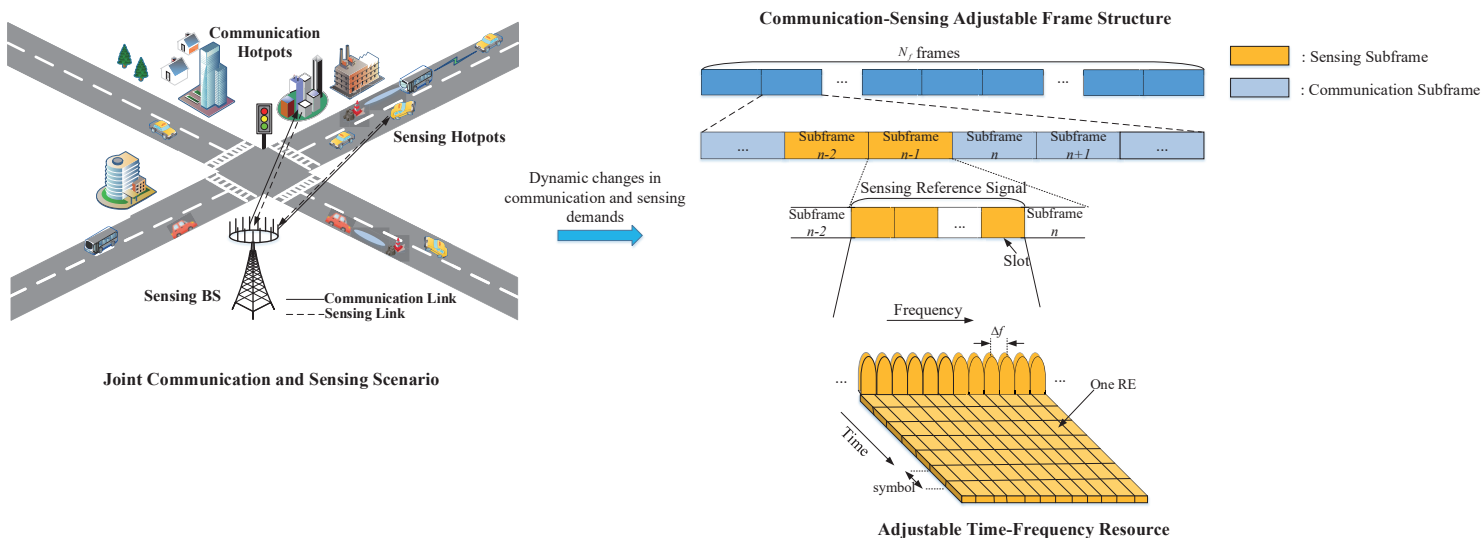


Fig. 17: Frame structure design for 5G-A and 6G

D. Inspiration of Frame Structure Design for 5G-A and 6G

The analysis of PRS for radar sensing shows that it is feasible for radar sensing and positioning. We provide some suggestions for the frame structure design of 5G-A and 6G in the future.

As shown in Fig. 17, we divide the frame structure into sensing subframe and communication subframe. The sensing subframe mainly realizes the function of radar sensing, and the communication subframe is mainly used for data transmission. It can also be used for radar sensing when the demand for sensing performance is high. Braun *et al.* [29] used the data of one OFDM frame for single target sensing. For massive downlink data transmission in large bandwidth, data signal can be used for sensing instead of sensing reference signal while serving communication users. However, when a single user transmits with partial bandwidth, the amount of data is small, so that the performance of sensing using data signal is poor [30]. Wild *et al.* [31] pointed out that although data symbols can be used for sensing, additional radar symbols are still required because there may be no data to transmit at a given time and direction where sensing needs to be performed. Barneto *et al.* [32] indicated that the communication transmitter is not always full-load, and there are usually unused subcarriers, which can be used by the radar subcarriers to improve the performance of radar sensing. Therefore, it is necessary to set the sensing reference signal specially used for radar sensing in the sensing subframe. Moreover, the power of pilot signal is high

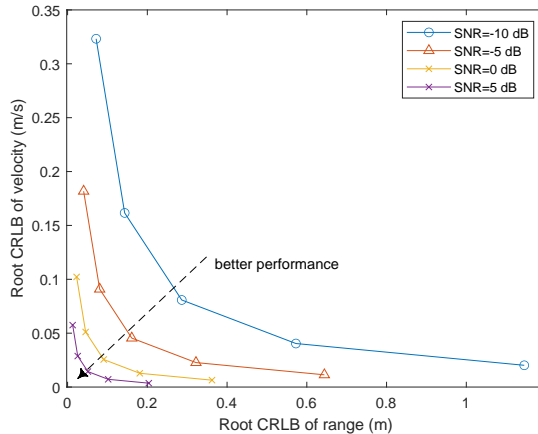


Fig. 18: The relationship between CRLB of range and velocity estimation

which has good anti-noise performance. In the scenario with high demand for sensing performance, the sensing reference signal and data signal are combined to realize long-distance sensing [33].

In order to realize adaptive communication and sensing performance, the design of sensing reference signal will support waveform reconfiguration to meet the requirements of sensing performance in different scenarios. In the scenario with low sensing performance requirements, the sensing reference signal can use the reference signal of the existing communication system, such as PRS, or redesign the sensing subframe by adjusting the time-frequency resources. Comb pattern is used to orthogonalize the frequency-domain allocation of sensing reference signals of users, which can not only meet the sensing performance required by diversified scenarios, but also further suppress the interference between BSs.

In the sensing subframe, the time-frequency resource allocation of the sensing reference signal is mainly determined by the sensing performance requirements. (32) and (33) show that there is a performance trade-off between range and velocity estimation. Fig. 18 shows the relationship between the CRLB of range and velocity estimation under different SNRs when the subcarrier spacing configuration μ is configured as 0, 1, 2, 3, 4. As the SNR increases, the CRLB of range and velocity estimation decreases, which indicates that a better lower bound of accuracy can be reached. The parameters such as Δf , N , M and f_c can be reasonably configured to satisfy the accuracy requirements for range and velocity estimation. In addition, the time-frequency resource mapping of the sensing reference signal can be flexibly adjusted to cope with different sensing scenarios. Take PRS for example, the different comb structures of PRS can prevent the interference of the PRS signals sent by multiple BSs.

In addition, in order to enhance the sensing performance, chirp [34, 35] and other frequency modulation schemes can be combined with OFDM to redesign the sensing reference signal. By increasing the time bandwidth product of the signal, the signal has higher resolution and accuracy.

VII. CONCLUSION

In this paper, we demonstrate the 5G PRS, as a pilot signal in 5G mobile communication system, has the feasibility and superiority in radar sensing compared with other pilot signals. We investigate the method of using 5G PRS for radar sensing to realize joint sensing, communication and positioning. Therefore, the PRS can be regarded as a sensing reference signal which requires no additional changes to the 5G signal, so that PRS for sensing can be well compatible with mobile communication system. We analyze the range and velocity estimation performance of PRS for radar sensing and derive the corresponding CRLB. Meanwhile, we also propose an enhanced method to improve the accuracy of velocity estimation using multiple frames. Simulation results show that the RMSE of the range and velocity estimation decrease with the increase of SNR. At the end of the paper, we also give some suggestions for the future 5G-A and 6G frame structure design, hoping to provide some inspirations for future frame structure design work.

ACKNOWLEDGMENT

The authors appreciate Future Research Lab at China Mobile Research Institute for the support to this research.

REFERENCES

- [1] Z. Wang, K. Han, J. Jiang, Z. Wei, G. Zhu, Z. Feng, J. Lu, and C. Meng. "Symbiotic sensing and communications towards 6G: Vision, applications, and technology trends," in *Proc. IEEE VTC 2021 fall*, Online Event, Sep. 2021.
- [2] Z. Feng, Z. Fang, Z. Wei, X. Chen, Z. Quan, and D. Ji. "Joint radar and communication: A survey," *China Communications*, vol. 17, no. 1, pp. 1–27, Jan. 2020.
- [3] M. L. Rahman, J. A. Zhang, X. Huang, Y. J. Guo and R. W. Heath, "Framework for a perceptive mobile network using joint communication and radar sensing," *IEEE Transactions on Aerospace and Electronic Systems*, vol. 56, no. 3, pp. 1926–1941, Jun. 2020.
- [4] <https://www.tonex.com/training-courses/introduction-to-6g-imt-2030/>.
- [5] J. A. Zhang, F. Liu, C. Masouros, R. W. Heath and A. Petropulu, "An overview of signal processing techniques for joint communication and radar sensing," *IEEE Journal of Selected Topics in Signal Processing*, pp. 1–1, Sep. 2021.
- [6] C. E. Cook. "Linear FM signal formats for beacon and communication systems," *IEEE Transactions on Aerospace and Electronic Systems*, vol. AES-10, no. 4, pp. 471–478, Jul. 1974.
- [7] X. Chen, X. Wang, S. Xu and J. Zhang, "A novel radar waveform compatible with communication," in *Proc. 2011 International Conference on Computational Problem-Solving (ICCP)*, Chengdu, China, pp. 177–181, Oct. 2011.
- [8] Peli Barrenechea, Frans Elferink, Johan Janssen, "FMCW radar with broadband communication capability," in *Proc. IEEE Proceedings of the 4 European Radar Conference*, Munich, Germany, pp. 130–133, Oct. 2007.
- [9] C. Sturm, T. Zwick and W. Wiesbeck, "An OFDM system concept for joint radar and communications operations," in *Proc. VTC Spring 2009 - IEEE 69th Vehicular Technology Conference*, Barcelona, Spain, pp. 1–5, 2009.
- [10] C. Sturm and W. Wiesbeck, "Waveform design and signal processing aspects for fusion of wireless communications and radar sensing," *Proceedings of the IEEE*, vol. 99, no. 7, pp. 1236–1259, Jul. 2011.
- [11] C. E. Shannon, "A mathematical theory of communication," *The Bell System Technical Journal*, vol. 27, no. 3, pp. 379–423, Jul. 1948.
- [12] H. Soury and B. Smida, "Optimal pilot overhead for FDD full-duplex communication and radar sensing (ComSens)," in *Proc. MILCOM 2017 - 2017 IEEE Military Communications Conference (MILCOM)*, Baltimore, MD, USA, pp. 725–730, Oct. 2017.
- [13] C. D. Ozkaptan, E. Ekici, O. Altintas and C. Wang, "OFDM pilot-based radar for joint vehicular communication and radar systems," in *Proc. 2018 IEEE Vehicular Networking Conference (VNC)*, Taipei, Taiwan, pp. 1–8, Dec. 2018.
- [14] P. Kumari, J. Choi, N. González-Prelcic and R. W. Heath, "IEEE 802.11ad-based radar: An approach to joint vehicular communication-radar system," *IEEE Transactions on Vehicular Technology*, vol. 67, no. 4, pp. 3012–3027, Apr. 2018.
- [15] G. Liu, H. Niu, M. Zheng, D. Bao, J. Cai, G. Qin, B. Wu, P. Li, and N. Liu. "Integration of communication and sar radar based on OFDM with channel estimation in high speed scenario," in *Proc. IGARSS 2019 - 2019 IEEE International Geoscience and Remote Sensing Symposium*, Yokohama, Japan, pp. 2519–2522, Jul. 2019.
- [16] C. D. Ozkaptan, E. Ekici and O. Altintas, "Demo: A software-defined OFDM radar for joint automotive radar and communication systems," in *Proc. 2019 IEEE Vehicular Networking Conference (VNC)*, Los Angeles, CA, USA, pp. 1–2, Dec. 2019.

- [17] D. Bao, G. Qin and Y. Dong, "A superimposed pilot-based integrated radar and communication system," *IEEE Access*, vol. 8, pp. 11520–11533, Jan. 2020.
- [18] C. -H. Wang, O. Altintas, C. D. Ozkaptan and E. Ekici, "Multi-range joint automotive radar and communication using pilot-based OFDM radar," in *Proc. 2020 IEEE Vehicular Networking Conference (VNC)*, New York, NY, USA, pp. 1–4, Dec. 2020.
- [19] M. L. Rahman, P. Cui, J. A. Zhang, X. Huang, Y. J. Guo and Z. Lu, "Joint communication and radar sensing in 5G mobile network by compressive sensing," in *Proc. 2019 19th International Symposium on Communications and Information Technologies (ISCIT)*, Ho Chi Minh City, Vietnam, pp. 599–604, Sep. 2019.
- [20] ITU-R WP5D Document 5D/400-E. DRAFT WORKING DOCUMENT TOWARDS A PRELIMINARY DRAFT NEW REPORT ITU-R M.[IMT.FUTURE TECHNOLOGY TRENDS OF TERRESTRIAL IMT SYSTEMS TOWARDS 2030 AND BEYOND] [S]. Geneva: ITU-R WP 5D, 2021.
- [21] <https://www.tonex.com/training-courses/introduction-to-5g-imt-2020/>
- [22] J. Li, S. An, J. An, H. Zirath and Z. S. He, "OFDM radar range accuracy enhancement using fractional fourier transformation and phase analysis techniques," *IEEE Sensors Journal*, vol. 20, no. 2, pp. 1011–1018, Jan. 2020.
- [23] 3GPP TS 38.211, "NR; Physical channels and modulation," V16.3.0, Oct. 2020.
- [24] 3GPP TS 38.214, "NR; Physical layer procedures for data," V16.5.0, Mar. 2021.
- [25] R. Morales Ferre, G. Seco-Granados, and E. S. Lohan, "Positioning reference signal design for positioning via 5G," in *Proc. XXXV Finnish URSI Convention on Radio Science URSI*, Oct. 2019.
- [26] L. Gaudio, M. Kobayashi, B. Bissinger and G. Caire, "Performance analysis of joint radar and communication using OFDM and OTFS," in *Proc. 2019 IEEE International Conference on Communications Workshops (ICC Workshops)*, Shanghai, China, pp. 1–6, May. 2019.
- [27] S. M. Kay, "Fundamentals of statistical signal processing," *PTR Prentice-Hall, Englewood Cliffs, NJ*, vol. 10, pp. 151045, 1993.
- [28] J. A. del Peral-Rosado, J. A. Lopez-Salcedo, G. Seco-Granados, F. Zanier and M. Crisci, "Achievable localization accuracy of the positioning reference signal of 3GPP LTE," in *Proc. 2012 International Conference on Localization and GNSS*, Starnberg, Germany, pp. 1–6, Jun. 2012.
- [29] M. Braun, C. Sturm and F. K. Jondral, "On the single-target accuracy of OFDM radar algorithms," in *Proc. 2011 IEEE 22nd International Symposium on Personal, Indoor and Mobile Radio Communications*, Toronto, Canada, pp. 794–798, Sept. 2011.
- [30] S. D. Liyanaarachchi, C. B. Barneto, T. Riihonen and M. Valkama, "Experimenting Joint Vehicular Communications and Sensing with Optimized 5G NR Waveform," in *Proc. 2021 IEEE 93rd Vehicular Technology Conference (VTC2021-Spring)*, Helsinki, Finland, pp. 1–5, Apr. 2021.
- [31] T. Wild, V. Braun and H. Viswanathan, "Joint design of communication and sensing for beyond 5G and 6G systems," *IEEE Access*, vol. 9, pp. 30845–30857, Feb. 2021.
- [32] C. B. Barneto, S. D. Liyanaarachchi, M. Heino, T. Riihonen and M. Valkama, "Full Duplex Radio/Radar Technology: The Enabler for Advanced Joint Communication and Sensing," *IEEE Wireless Communications*, vol. 28, no. 1, pp. 82–88, Feb. 2021.
- [33] A. Tang, S. Li, and X. Wang, "Self-Interference-Resistant IEEE 802.11ad-Based Joint Communication and Automotive Radar Design," *IEEE Journal of Selected Topics in Signal Processing*, vol. 15, no. 6, pp. 1484–1499, Nov. 2021.
- [34] M. Li, W. Wang, Z. Zheng, "Communication-embedded OFDM chirp waveform for delay-Doppler radar," *IET Radar, Sonar & Navigation*, vol. 12, no. 3, pp. 353–360, Dec. 2017.
- [35] D. Dash, A. Jayaprakash, Valarmathi J and G. R. Reddy, "Generalized OFDM-LFM waveform design and analysis for multistatic airborne radar," in *Proc. 2015 IEEE Power, Communication and Information Technology Conference (PCITC)*, Bhubaneswar, India, 2015, pp. 924–929.